Correcting land surface temperature data for elevation and illumination effects in mountainous areas: A case study using ASTER data over a steep-sided valley in Morocco

Yoann Malbéteau, Olivier Merlin, Simon Gascoin, Jean-Philippe Gastellu-Etchegorry, C Mattar, Luis Enrique Olivera-Guerra, S P Khabba, Lionel Jarlan

Correcting land surface temperature data for elevation and illumination effects in mountainous areas: a case study using ASTER data over a steep-sided valley in Morocco

Malbéteau Y.[1], O. Merlin[1,2], S. Gascoin[1], J.P. Gastellu[1], C. Mattar[3], L. Olivera-Guerra[3], S. Khabba[2], L. Jarlan[1]

[1] *Centre d'Etudes Spatiales de la Biosphère (CESBIO), 18 Avenue, Edouard Belin, bpi 2801, 31401 Toulouse Cedex 9, France*
[2] *Faculté des Sciences Semlalia, Université Cadi Ayyad (UCAM), Avenue Prince Moulay Abdellah, BP 2390, Marrakech 40000, Morocco*
[3] *Laboratory for Analysis of the Biosphere (LAB), University of Chile, Avenidad Santa Rosa 11315, La Pintana, Santiago, Chile*

yoann.malbeteau@cesbio.cnes.fr, +212 5 24 43 16 26

Abstract

The remotely sensed land surface temperature (LST) is a key parameter to monitor surface energy and water fluxes but the strong impact of topography on LST has limited its use to mostly flat areas. To fill the gap, this study proposes a physically-based method to correct LST data for topographic -namely illumination and elevation- effects over mountainous areas. Both topographic effects are first quantified by inverting a dual-source soil/vegetation energy balance (EB) model forced by 1) the solar radiation simulated by a 3D radiative transfer model named DART (Discrete Anisotropic Radiative Transfer) that uses a Digital Elevation Model (DEM), 2) a satellite-derived vegetation index, and 3) local meteorological (air temperature, air relative humidity and wind speed) data available at a given location. The satellite LST is then corrected for topography by simulating the LST using both pixel- and image-scale DART solar radiation and elevation data. The approach is tested on three ASTER (Advanced Spaceborne Thermal Emission and Reflection Radiometer) overpass dates over a steep-sided 6 km by 6 km area in the Atlas Mountain in Morocco. The mean correlation coefficient and root mean square difference (RMSD) between EB-simulated and ASTER LST is 0.80 and 3°C, respectively. Moreover, the EB-based method is found to be more accurate than a more classical approach based on a multi-linear regression with DART solar radiation and elevation data. The EB-simulated LST is also evaluated against an extensive ground dataset of 135 autonomous 1-cm depth temperature sensors deployed over the study area. While the mean RMSD between 90 m resolution ASTER LST and localized ibutton measurements is 6.1°C, the RMSD between EB-simulated LST and ibutton soil temperature is 5.4 and 5.3°C for a DEM at 90 m and 8 m resolution, respectively. The proposed topographic correction is self-calibrated from (LST, DEM, vegetation index and in situ meteorological data) data available over large extents. and could potentially be used in conjunction with evapotranspiration retrieval methods based on LST.

Keywords: Land surface temperature, topographic correction, ASTER, Energy Balance, DART, DEM

1. Introduction

The radiative skin temperature over land or land surface temperature (LST) plays an important role in the physics of surface-atmosphere interactions. It is at the same time a driver and a signature of the energy and mass exchanges over land (Anderson et al., 2008; Brunsell and Gillies, 2003; Karnieli et al., 2010; Kustas and Anderson, 2009; Zhang et al., 2008). LST is highly variable in both space and time (Prata et al., 1995), mainly as a result of the heterogeneity of the meteorological forcing, land cover, soil water availability, surface radiative properties and topography. Therefore, satellite-derived LST is widely used in a variety of applications including evapotranspiration monitoring (Bastiaanssen et al., 1998; Boulet et al., 2007), climate change studies (Hansen et al., 2010), soil moisture estimation (Sandholt et al., 2002; Merlin et al., 2010a), vegetation monitoring (Kogan, 2001), urban climate studies (Voogt and Oke, 2003) and forest fire detection (Eckmann et al., 2008).

Since LST and soil water availability are coupled under non energy-limited conditions, LST has been used as a proxy of the surface water status in combination with energy balance modeling (Norman et al., 1995; Anderson et al., 2008; Kustas and Anderson, 2009; Merlin et al., 2010a; Bastiaanssen et al., 1998; Allen et al., 2007; Boulet et al., 2007; Mattar et al., 2014; Cammalleri and Vogt, 2015). All those studies have focused on relatively flat regions to facilitate the interpretation of the LST variability associated with the surface parameters, fluxes or processes of interest. Over hilly areas, the application of such approaches is limited because the signature of the surface water status on LST is masked by topography effects, namely the pixel-scale impact of illumination (solar radiation) and elevation (air temperature) on LST. Especially, temperature differences between south-facing and north-facing slope can reach 30°C (Shreve, 1924; Raz-Yaseef et al., 2010) due to illumination effects. Globally, about 20% of continental surfaces consist of mountainous terrain (Meybeck et al., 2001) where LST is significantly impacted by topography. However, to our knowledge, there is no method to correct the remotely sensed LST for the topography-induced atmospheric forcing variability, that is to derive the LST that would be observed under uniform solar radiation and air temperature conditions.

Note that the retrieval of LST from satellite observations over mountainous areas is subject to uncertainties associated with viewing geometry i.e. GIFOV (ground instantaneous field of view) and the anisotropic nature of emissivity. Modeling, experimental, and case studies have reported an anisotropic effect on LST typically ranging from 1 to 2°C depending on the pixel-scale radiometer viewing angle and up to 3°C for extreme viewing angles (Lagouarde et al., 1995; Sobrino and Cuenca, 1999; Minnis and Khaiyer, 2000; Coret et al., 2004; Rasmussen et al., 2010; Proy et al., 1989; Liu et al., 2006, 2009). The LST retrieval errors due to viewing geometry are thus much smaller (<10%) than the potential impact of topography-induced atmospheric forcing variability on LST. At the subpixel scale, current LST retrieval methods overlook the (commonly unresolved) fine-scale surface roughness (Danilina et al., 2012, 2013).

To assess the impact of topography on remotely sensed LST, previous studies have attempted to simulate LST over mountainous areas. For example, Hais and Kučera (2009) simulated LST using linear regressions with the hillshade computed by the spatial analyst toolbox of ArcGis based on a DEM (Digital Elevation Model). The surface energy balance (EB) equation has also been used over mountainous terrain to simulate LST (Dozier and Outcalt, 1979). Originally, this approach was designed for bare soil or low grassy vegetation with a single source EB model using a topographic map and a set of ancillary (incoming solar radiation, albedo, wind speed, air temperature, surface roughness length and relative air humidity) measurements. The variability of albedo was estimated with soil wetness and illumination angle information, while the variation of air temperature with elevation was estimated using the standard environmental lapse rate of -6.5°C.km^{-1}. In Dozier and Outcalt (1979), wind speed and relative air humidity were assumed to be homogeneous over the study area. The incoming solar radiation was computed for each grid cell according to the local solar incidence angle and a diffuse radiation factor. However, the solar radiation in their model did not include the diffuse reflection from adjacent terrain.

Later Rigon et al. (2006) developed a distributed hydrological model that accounts for complex topography. This model named GEOtop describes the energy and mass exchanges at the surface/atmosphere interface by taking into account 1) the impact of elevation on air temperature, 2) the effects of slope/exposure on solar radiation and 3) the spatial distribution of vegetation and soil water content. In that study, the EB model of GEOtop is single source. It is forced by temperature and wind speed measurements, which are regionalized over the study area. The incoming direct shortwave radiation is computed for each grid cell according to the local solar incidence angle, including the diffuse radiation due to atmospheric and cloud transmissivity. This model also includes shadowing effects of direct solar radiation by the surrounding mountains. In that paper, shadowing was basically expressed as a factor ranging

from 0 if the grid cell is completely in shadow (no direct radiation) to 1 if the sun radiation hits the surface. More recently Bertoldi et al. (2010) and Endrizzi et al. (2013) used the same (GEOtop) model to estimate the topographical effects on soil temperature simulations for different applications including ecohydrology, soil freezing and snow cover assessment.

To simulate LST accurately using an EB model, the incoming solar radiation should be represented at the pixel scale (Allen et al., 2006). The solar radiation (noted Rg in $W.m^{-2}$) reaching the surface at a given location is the sum of direct solar radiation, diffuse sky radiation, and the direct and diffuse radiations reflected by nearby terrains (Dubayah, 1994). Rg mainly depends on the cloud cover, the turbidity of the clean air, the time of year, latitude, albedo of the surrounding terrain and surface geometry (Essery and Marks, 2007). Estimating the Rg variability over mountainous areas is challenging due to the irregular topographic geometry of the surface and to the multiple reflections that occur in such conditions. At high resolution, the variability in slope angles and slope orientations, as well as the shadows cast by topographic agents can lead to strong local gradients in Rg (Dozier, 1980; Dubayah, 1992). Moreover, since the in situ monitoring network ineffectively covers the complex heterogeneity of mountainous areas, simple geostatistical methods for spatial interpolation of solar radiation are not always representative enough. Consequently, algorithms that explicitly or implicitly account for the features creating strong local gradients in the incoming radiation must be applied (Susong et al., 1999; Garen and Marks, 2005). The most advanced method to compute the distributed Rg over a landscape is to use a 3D radiative transfer model, which explicitly simulates its three components: direct solar radiation, diffuse sky radiation and reflected radiations. Here we used DART model (Discrete Anisotropic Radiative Transfer, Gastellu-Etchegorry et al. (1996)) as one of the most comprehensive physically based 3D models simulating the Earth-atmosphere radiation interaction from visible to thermal infrared wavelengths.

In this context, this study aims to develop an original method to correct the remotely sensed LST for topography-induced atmospheric forcing (solar radiation and air temperature) variability. This method uses an EB model forced by the solar radiation derived from DART and the air temperature gradient derived from elevation data. The approach is tested at 90 m resolution using ASTER (Advanced Spaceborne Thermal Emission and Reflection Radiometer) data over a 6 km by 6 km steep-sided area in the Moroccan Atlas. The LST is corrected for topography by simulating the LST using DART solar radiation and elevation data. Moreover, the EB approach is implemented using a dual source formulation, allowing for a representation of topographic effects on both soil and vegetation components. Three different strategies are proposed to evaluate the correction approach. First, the EB model is compared in terms of simulated LST with two other simpler approaches based on the same input (DART solar radiation and elevation) data. Second, the LST simulated by the EB model is evaluated against a set of soil temperature measurements distributed at 45 points within the study area. Third, the quality of corrected LST is analyzed both qualitatively and quantitatively.

2. Study materials

2.1. Study region

The High Atlas is a Moroccan mountain chain of approximately 60 km in width and 800 km in length organized along a NE-SW axis. It culminates at 4167 m above sea level at the Jbel Toubkal, the highest summit of North Africa. The central part of the High-Atlas is the water tower for the northern semi-arid plains of the Tensift catchment, Marrakech region (Chehbouni et al., 2008). The experimental data set was collected over the Imlil valley (31.12°N; 7.93°W) part of the Rheraya sub-catchment (Toubkal national park). This valley has an East-West orientation, thus maximizing the solar exposure effects on LST. It covers a surface area of about $\backsim 9$ km^2 (Fig. 1) and is characterized by a semi-arid and mountainous climate. The annual precipitation is about 600 mm /year with intense events in winter and sparse localized thunderstorms during spring and summer. The vegetation cover is a function of elevation and human activity, so that dense vegetation is observed along the stream valley only. Others areas are characterized by bare or poorly vegetated loam gravelly brown soil. Terrain elevation varies between 1700 and 3150 m and hillslope range between 0 (stream valley) and 70 (highest elevation) degrees. Such conditions offer an interesting test site for developing and testing methods for LST topographic correction . The study region covers an area of 6 km x 6 km including the Rheraya sub-catchment (Fig. 1).

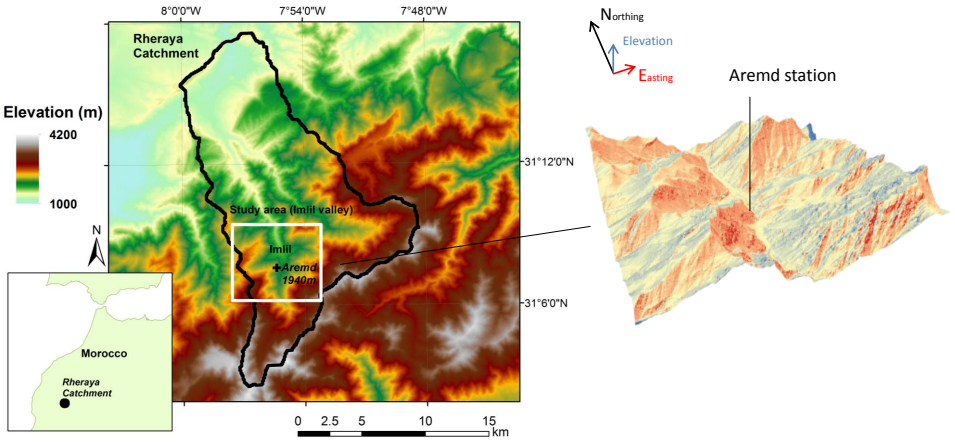

Figure 1: On the left, location of the Rheraya catchment, the Imlil subcatchment, and the study area. On the right, a 8 m resolution 3D DEM over the study area indicating the sun-facing (red) and shaded (blue) slopes at 11:30 am local time (GMT).

2.2. *Remote sensing data*

2.2.1. *ASTER land surface temperature*

ASTER is one of the five scientific instruments onboard the satellite platform Terra, part of NASAs Earth Observation System (EOS). ASTER is a high spatial resolution radiometer, which consists of three separate subsystems: the visible and near infrared, the shortwave infrared and the thermal infrared. The multispectral TIR (Thermal InfraRed: 5 channels between 8 and 12 μm) allows the retrieval of LST and emissivity spectra at high spatial (90 m) resolution (Abrams, 2000). The LST data used in this study are extracted from the on-demand surface kinetic temperature AST_08 product (Gillespie et al., 1998). This product is derived using the same algorithm as the Surface Emissivity Product. Surface kinetic temperature is determined by applying Planck's Law using the emissivity values from the Temperature-Emissivity Separation algorithm. ASTER surface radiance data are corrected from radiometric (sun spot, shading), atmospheric and geometric effects (Gillespie et al., 1998; Abrams, 2000). Absolute accuracy of LST product is about 2°C (Gillespie et al., 1998; Abrams, 2000; Liu et al., 2006). Note that a major source of error is due to the use of a 1 km DEM for atmospheric correction (Gillespie et al., 1998). ASTER products were acquired specifically on the study area at 11:22 am UTC on 3 dates: April 14^{th} and 30^{th} and September 5^{th}, 2014.

2.2.2. *Digital elevation models*

In this study two DEMs were used with an original spatial resolution of 30 and 4 m. NASA and the Ministry of economy, Trade and Industry of Japan (METI) produced the global 30 m grid size ASTER GDEM product. The GDEM v2 released in October 2011, it is an improved version of GDEM v1 released in June 2009 with an absolute vertical and horizontal accuracy of 17 and 30 m (Meyer, 2011), respectively. The 4 m resolution Pleiades DEM is also used. The Pleiades 1A and 2B twin satellites were launched 17 December 2011 and 2 December 2012, respectively. The DEM was derived from Pleiades-1A stereoscopic pairs acquired over the Rheraya catchment on the 18^{th} of August 2015 at 11:19 am (within a few tens of seconds due to the agility of the platform). Images are delivered at a ground sampling distance of 0.5 m for the panchromatic channel. The DEM was generated through the Automatic Terrain Extraction algorithm in the ERDAS Imagine 2014 photogrammetry toolbox. Three accurate wide-spread control points were collected in the images area. One of them located near the Imlil valley was used as an absolute horizontal ground control point to improve the horizontal geolocation accuracy. Pixel size is of 4 m, which is a good compromise between processing time and DEM accuracy (Berthier et al., 2014; Marti et al., 2014). The accuracy of the DEM horizontal registration was evaluated based on two other check points obtained by geodesic GPS. The error was lower than 4 m in both cases. The vertical error was evaluated based on all three points and was between 1 m and 5 m. The hillshaded raster generated from the Pleiades DEM was also inspected in the Imlil valley region and we found no artifacts or aberrations due to the stereo-correlation. Note that the 4 m resolution DEM was resampled to

8 m using cubic interpolation due to computer memory limitation of DART model when simulating the 3D radiative budget of the whole study area at spatial resolution better than 8 m. This situation will be improved in next DART version with new data format and the possibility to work with pixels that can have different dimensions within the same scene.

2.2.3. Remotely sensed vegetation index

The vegetation cover is derived over the study area from the 30 m resolution Landsat data collected on dates closest to the three ASTER overpass dates. The Landsat reflectances Claverie et al. (2015)) were used to compute the Normalized Difference Vegetation Index (NDVI), defined as the ratio of the difference between near-infrared and red reflectances to their sum. Fractional vegetation cover (fv) is estimated as in Gutman and Ignatov (1998):

$$fv = \frac{NDVI - NDVI_s}{NDVI_{vg} - NDVI_s} \tag{1}$$

with $NDVI_{vg}$ corresponding to fully-covering vegetation and $NDVI_s$ to bare soil. In this study, $NDVI_{vg}$ and $NDVI_s$ are set to the maximum and minimum value of the NDVI observed within the study domain, respectively. Several studies have investigated the spatial scale dependencies of NDVI and the relationship between NDVI and fv. As a first approximation, we consider that the first-order estimate, proposed by Gutman and Ignatov (1998), adequately describes the relationship.

2.3. Ground Data

2.3.1. Meteorological data

Meteorological data including air temperature, relative air humidity and wind speed have been measured every minute and the averages have been acquired every half hour since May 2003 at Imlil station (31.124875°N; 7.920458°W) located close to the center of the study area at an elevation of 1970 m (Fig. 1). Data have been collected and processed in the frame of the Joint International Laboratory TREMA, Marrakech-Morocco (Jarlan et al., 2015).

2.3.2. Temperature sensors/loggers

The ibutton sensor (model DS1921G) is a coin size that integrates a micro-controller, 2kB storage, a real-time clock, a temperature sensor, and a battery. The ibutton temperature sensors measure temperature in 0.5°C increments from -30°C to 70°C with ± 1°C accuracy (Hubbart et al., 2005).

In 2014, a total of 135 ibuttons were deployed over the Imlil valley to cover a range of solar exposures and elevations (Fig. 2). 102 ibuttons were installed on the 3^{rd} April 2014, set up across both sides of the valley to provide a spatial understanding of illumination effects on LST. To complete the spatial distribution, 33 additional ibuttons were set up on the 7^{th} May 2014 across a third slope. All sensors were removed on the 2^{nd} October 2014 (approximately 6 months later) before the first snowfall events in the area. In practice, ibuttons were installed 3 by 3 on a 7 by 7 cm thin transparent plastic plate to prevent spreading down into the slope and variations in placement. They were pinned in a topographic environment that was relatively homogeneous at 90 m scale with different illumination and elevation (Fig. 2). The resulting 45 plates were buried very close (~1 cm) to the soil surface by making sure that ibuttons were not directly exposed to solar radiation. We are aware that plates disturb, at least a little bit, surface moisture and latent heat, however it is difficult to estimate impact on the measures. The recording time resolution (135 minutes) for each sensor was chosen based on the maximum ibutton data storage for a 6 month recording. However, the three ibuttons of a given plate were recording temperature with a 45 minute delay between each acquisition, so that the recording time resolution of each plate (by combining all three ibuttons sensors) was 45 minutes. Each plate was installed along transects at a regular spacing of about 150 m (Fig. 2). The locations were recorded using handheld GPS measurements (accuracy ± 6 m) and were physically marked by a white cairn for easier recovery. Every retrieved ibutton (42/45 plates) recorded valid data; and one plate reappeared on the surface and was excluded from the analysis. In total, 91% of the ibuttons installed data could be used for the analysis.

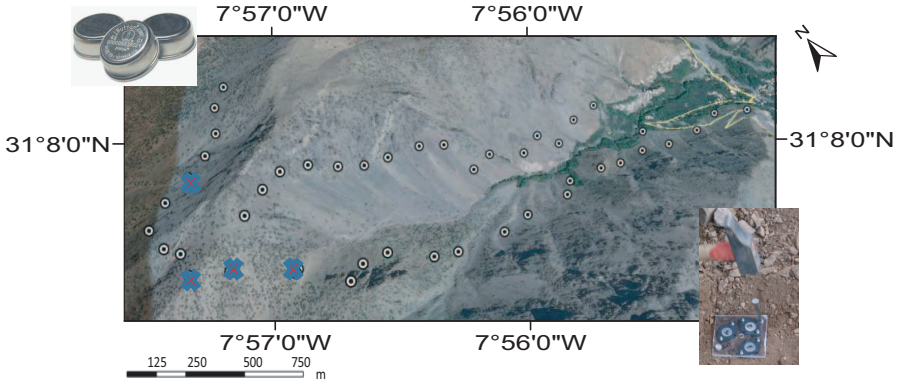

Figure 2: Locations of the 45 ibutton plates, each of them containing 3 ibutton sensors. Red cross indicate plates not used for the study.

2.4. DART model

DART is one of the most complete 3D models designed for simulating the radiative budget and the satellite observations of the land surface in the visible, near infrared and thermal infrared bands. It simulates the radiative transfer in heterogeneous 3D landscapes with the exact kernel and discrete ordinate methods (Gastellu-Etchegorry et al., 2004). Any landscape is simulated as a rectangular matrix of parallelepipedic cells, i.e. building blocks for simulating larger scenes. In this work, the DART model (version 5.5.3) is used to simulate the solar radiation or illumination (noted Rg in $W.m^{-2}$) at the surface for any location in the study valley. One main advantage of DART is to compute the three components of incoming total solar radiation ($W/m^2/\mu m$) of any rugged terrain surface: direct solar radiation, diffuse sky radiation and the (direct and diffuse) reflected radiations from the adjacent surfaces. The reflected radiation is modulated by the reflectance spectra of the surfaces. In practice, surface irradiance depends on the relative orientation of incident rays and the local slope, which explains why DART uses a DEM, time and geographic coordinates as input parameters. DART simulations were conducted for the visible and near infrared spectral domains (0.4 μm to 1.1 μm) that is representative images of Rg. In that spectral band, the irradiance varies between 100 and 1800 $W.m^{-2}$ over the simulated scene (Fig. 3). The capability of the DART has been successfully tested in a number of works in the visible and near-infrared spectral domains (Widlowski et al., 2007, 2008). Then, the DART model has been evaluated in the thermal range, where works have addressed the usefulness of this model (Guillevic et al., 2003; Gastellu-Etchegorry, 2008; Sepulcre-Cantó et al., 2009; Sobrino et al., 2011). However the DART capability has not been evaluated to simulate solar radiation, particularly in mountainous area, due to the difficulty to get such data. Therefore, there is no way to estimate directly the accuracy of DART results.

3. Topographic normalization methods

The methodologies presented in this section aim to correct ASTER LST data for topographic including illumination and elevation- effects. Elevation is derived from the 30 m resolution GDEM and is then aggregated at ASTER (90 m) resolution. The incoming solar radiation received at the surface is simulated by DART at the three ASTER overpass dates. Both elevation and DART-simulated illumination are used as input to topographic correction . The approach is based on the EB equations for soil and vegetation, and compared to two different approaches based on 1) a multi-linear regression between ASTER LST, elevation and DART irradiance map, and 2) the slope of the dry edge of both ASTER LST-E (elevation) and ASTER LST-Rg feature spaces.

3.1. Topographic normalization based on the soil and vegetation Energy balance equations

The proposed correction methodology was originally developed in Merlin et al. (2005) to improve the disaggregation of coarse-scale soil moisture data using LST data available at higher spatial resolution. The correction method was further applied to the disaggregation of kilometric LST data over flat irrigated areas (Merlin et al., 2010b). In

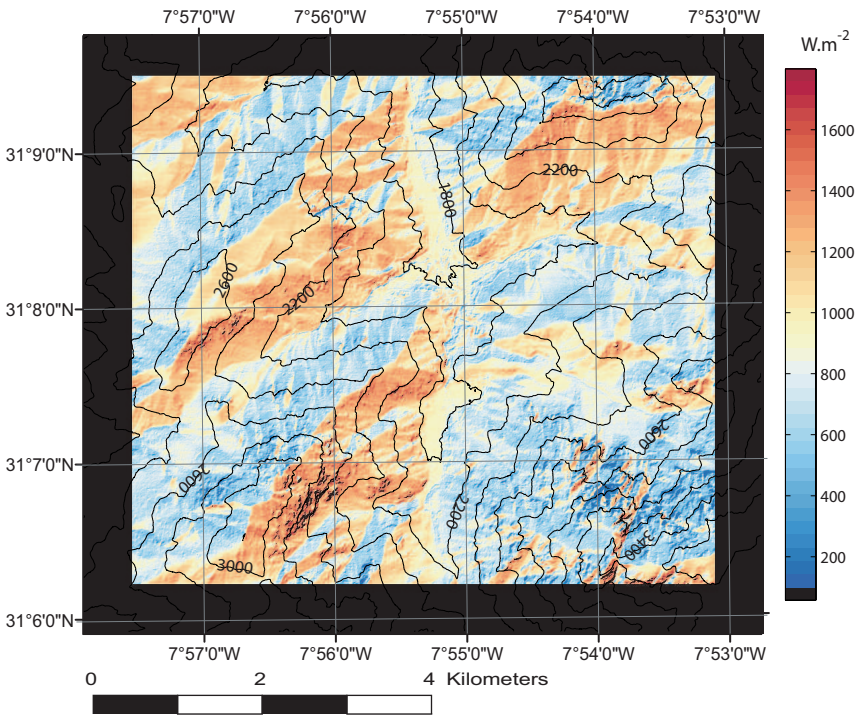

Figure 3: DART simulated irradiance over [0.4μm- 1.1μm] of the whole study area (white square in Fig. 1), with 8m resolution DEM at 11:22 am (UTC) on September 5, 2014. Black lines represent the elevation contour lines between 1800 and 3600 m with a 200 m increment.

this paper, the technique is implemented to correct satellite (ASTER) LST data for topographic effects at the spatial resolution of available DEMs. The correction model is written as:

$$T_{corr,EB} = T_{ASTER} + T_{EB}(E, Rg) - T_{EB}(\langle E\rangle, \langle Rg\rangle) \quad (2)$$

With $T_{corr,EB}$ in °C being the ASTER LST corrected for topographic effects using the EB approach, T_{ASTER} in °C being the ASTER LST, $T_{EB}(E, Rg)$ in °C the LST simulated by the EB equations using pixel-scale elevation (E) in m and solar radiation (Rg) in W.m^{-2}, and $T_{EB}(\langle E\rangle, \langle Rg\rangle)$ in °C the LST simulated by the EB equations using the average of E ($\langle E\rangle$) and Rg ($\langle Rg\rangle$) at the image scale. LST is estimated as a linear function of component temperatures (Merlin and Chehbouni, 2004; Anderson et al., 2008; Long and Singh, 2012).

$$T_{EB} = fv \times Tv_{EB} + (1 - fv) \times Ts_{EB} \quad (3)$$

with Tv_{EB} in °C being the vegetation temperature and Ts_{EB} in °C the soil temperature. The soil temperature is expressed as:

$$Ts_{EB} = fss \times T_{s,dry_{EB}} + (1 - fss) \times T_{s,wet_{EB}} \quad (4)$$

with $T_{s,dry_{EB}}$ in °C the soil temperature in dry condition, $T_{s,wet_{EB}}$ in °C the soil temperature in wet condition and fss a dryness index of the soil surface. fss equals to 1 when the soil is fully dry (surface soil moisture close to the residual value) and to 0 when the soil is fully wet (surface soil moisture close to the soil moisture at saturation). Similarly, the vegetation temperature is expressed as:

$$Tv_{EB} = fsv \times T_{v,dry_{EB}} + (1 - fsv) \times T_{v,wet_{EB}} \quad (5)$$

with $T_{v,dry_{EB}}$ in °C the temperature of fully stressed (non-transpiring) vegetation, $T_{v,wet_{EB}}$ in °C the temperature of a vegetation that is unstressed (transpiring at the potential rate) and fsv a vegetation water stress index. fsv is equal

to 1 when the root zone soil moisture is above field capacity and to 0 when the root zone soil moisture is below the wilting point.
Dry bare soil, wet bare soil, fully stressed and unstressed vegetation extreme temperatures are then derived by solving the EB equation for each case, as described below. The dry bare soil EB equation is written as:

$$Rn_{s,dry} - Gdry = H_{s,dry} \tag{6}$$

with $Rn_{s,dry}$ (W.m^{-2}) being the net radiation from dry soil, $Gdry$ (W.m^{-2}) the ground heat in dry condition and $H_{s,dry}$ (W.m^{-2}) the sensible heat of dry soil. Similarly the wet bare soil EB equation is written as:

$$Rn_{s,wet} - Gwet = H_{s,wet} + LE_{s,wet} \tag{7}$$

with $Rn_{s,wet}$ (W.m^{-2}) being the net radiation from wet soil, $Gwet$ (W.m^{-2}) the ground heat in wet condition, $H_{s,wet}$ (W.m^{-2}) the sensible heat of wet soil and $LE_{s,wet}$ (W.m^{-2}) the latent heat of wet soil. The fully-stressed vegetation EB equation is written as:

$$Rn_{v,dry} = H_{v,dry} \tag{8}$$

with $Rn_{v,dry}$ (W.m^{-2}) and $H_{v,dry}$ (W.m^{-2}) being the net radiation and the sensible heat of water-stressed vegetation, respectively. Hence, the unstressed vegetation EB equation is written as:

$$Rn_{v,wet} = H_{v,wet} + LE_{v,wet} \tag{9}$$

with $Rn_{v,wet}$ (W.m^{-2}), $H_{v,wet}$ (W.m^{-2}) and $LE_{v,wet}$ (W.m^{-2}) being the net radiation, sensible heat, and latent heat flux of unstressed vegetation, respectively. The expressions of each flux component of the above EB equations are detailed in the appendix A .
In EB equations 4 and 5, the air temperature (Ta) at the pixel scale is estimated as:

$$Ta = Ta_{station} + LR \times (E - E_{station}) \tag{10}$$

with $Ta_{station}$ (°C) is the air temperature measured at the Imlil meteorological station, E (m) the pixel elevation, $E_{station}$ (m) the elevation of the station, and LR the environmental lapse rate (°C. m^{-1}). The latter is defined as the rate at which air temperature decreases with increasing elevation. LR is estimated at image-scale for each ASTER overpass date separately.

The four temperatures (Ts,dry, Ts,wet, Tv,dry and Tv,wet) in eq. 4 and 5 are solved numerically using the Newton′s method (Bristow, 1987). The convergence of component temperature is assumed to be reached when the absolute temperature difference between two consecutive iterations is lower than a given threshold (set to 0.01 °C).

Given that ASTER LST observations are available to calibrate the topographic correction model; three additional constraints are applied to the LST model in eq. 3. The first step consists in removing any possible bias in $T_{EB}(E, Rg)$ and T_{EB} ($\langle E \rangle$, $\langle Rg \rangle$):

$$T_{EB} = \langle T_{ASTER} \rangle + T_{EB} - \langle T_{EB} \rangle \tag{11}$$

with $\langle T_{ASTER} \rangle$ and $\langle T_{EB} \rangle$ being the average of T_{ASTER} and T_{EB} over the study area, respectively.

The second step consists in adjusting fss and fsv in equations 4 and 5 by minimizing the RMSD (Root Mean Square Difference) between ASTER LST and model-derived LST, for each ASTER overpass date separately. The third step consists in adjusting LR in eq. 10 by minimizing the RMSD between ASTER LST and model-derived LST. Note that the two latter steps require running the LST model at the observed LST resolution, which is the ASTER resolution in our case. Once the LST model has been calibrated in mean value and via the LR parameter, it can be applied to any spatial resolution, provided a DEM is available at the target resolution. The above calibration needs initializing LR with a LR first-guess of -6°C.km^{-1}, according to Glickman and Zenk (2000). The algorithm is summarized in Fig. 4.
The above correction method is based on several assumptions. Air humidity and wind speed (from the Imlil station data) are assumed to be uniform within the study area. The surface parameters εs, εv, αs and αv are also assumed to be homogeneous within the study area. αs and αv are estimated as the mean of the 1 km resolution MODIS-derived albedo (MCD43B3 product) over the study area. εs, εv are set up to 0.96 and 0.98, respectively, according to look-up tables from Rubio et al. (2003).

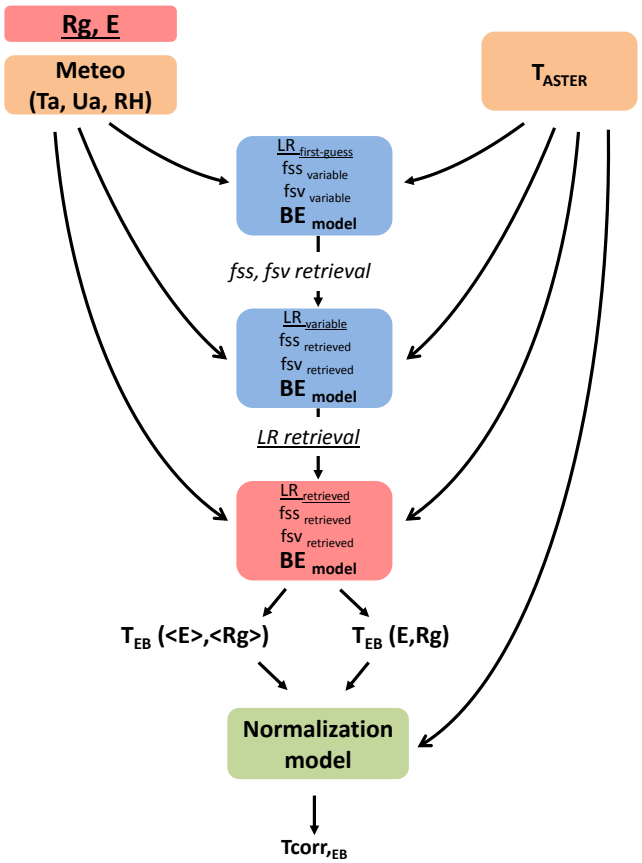

Figure 4: Schematic diagram presenting an overview of the topographic correction approach based on EB equations. The EB model (originally designed for solving mix-pixel problem in lowlands) is adapted to mountainous environment, and changes are highlighted by red boxes and underlined variables.

3.2. *Topographic normalization based on multi-linear regression*

The second proposed correction model is based on multilinear (ML) regression:

$$T_{corr,ML} = T_{ASTER} - (T_{ML} - \langle T_{ML} \rangle) \tag{12}$$

with $T_{corr,ML}$ being the ASTER LST corrected for topographic effects using the ML approach, and T_{ML} the LST simulated by the ML regression using T_{ASTER}, DEM-derived E and DART-simulated Rg :

$$T_{ML} = \langle T_{ASTER} \rangle + A_E(E - \langle E \rangle) + A_{Rg}(Rg - \langle Rg \rangle) \tag{13}$$

with A_E and A_{Rg} being two linear regression coefficients associated to E and Rg, respectively. A_E and A_{Rg} are computed for each image separately. The above correction method is based on several assumptions. Both variables Rg and E are assumed independent from each other because the ML regression can only fit observed data (LST ASTER) using a linear combination of independent variables (E and Rg). However, the latter assumption is considered valid only if the scene has the whole aspect range (between 0 to 360° slope orientation). The ML approach also assumes that each pixel of the scene has the same behavior in term of illumination and elevation. In other words, the ML approach represents identically the topographic effects on both soil and vegetation components.

3.3. Topographic normalization based on the slope of dry edges

Originally proposed by Goward et al. (1985), the space-based approach, also known as the triangle/trapezoidal method, uses the contextual information contained in remotely sensed LST and a vegetation index to estimate evapotranspiration. This method was subsequently utilized to monitor soil water content (Sandholt et al., 2002; Merlin et al., 2008; Kim and Hogue, 2012; Sobrino et al., 2012), surface resistance (Nemani and Running, 1989), land use and land cover change (Julien and Sobrino, 2009) and drought (Wan et al., 2004). Recently, Merlin (2013) combined the LST-albedo space and the LST-NDVI spaces, by taking advantage of the complementarity of NDVI and albedo data for evapotranspiration estimation. (Merlin, 2013).

Following this study, both LST-E and LST-Rg spaces provide complementary information on the spatial variation of LST in mountainous areas. The space-based approach thus potentially offers an interesting alternative method to correct LST for topographic effects. In space-based methods, usually implemented over flat areas, the lower edge corresponds to mostly wet pixels, while the upper edge is associated with dry pixels. In mountainous areas, it is often observed that vegetation occupies specific locations, such as the valley bottom and/or the lowest elevations. The Imlil valley includes contrasted conditions between the irrigated crops at the relatively flat valley bottom, and the surrounding dry bare soil slopes. Therefore, it is expected that vegetated areas do not cover a large range of illumination and elevation conditions. For this reason, the third proposed topographic correction model is based on the dry edge (upper limit) of the LST-E and LST-Rg spaces (Fig. 5). In the same way as for the EB and ML method, the correction model is written as:

$$T_{corr,DE} = T_{ASTER} - (T_{DE} - \langle T_{DE} \rangle) \tag{14}$$

with $T_{corr,DE}$ being the ASTER LST corrected for topographic effects based on the slope of dry edges (DE), and T_{DE} the LST simulated by the DE approach using T_{ASTER}, DEM-derived E and DART-simulated Rg :

$$T_{DE} = \langle T_{ASTER} \rangle + B_E(E - \langle E \rangle) + B_{Rg}(Rg - \langle Rg \rangle) \tag{15}$$

with B_E being the slope of the DE in the LST-E space, and B_{Rg} the slope of the DE in the LST-Rg space. B_E and B_{Rg} are computed for each image separately.

The approach proposed by Menenti et al. (1989) is used to determine the slope of the DE in the LST-E space. It is computed as the slope of the linear regression of the maximum LST determined for each E class and by excluding the E values below a threshold which does not take into account the LST variation due to the Rg effects. The threshold of E is constrained as the maximum LST simulated by the third order polynomial, estimated by using the maximum LST value of each E class (Fig. 5). Similarly, the slope of the DE in the LST-Rg space is computed as the slope of the linear regression of the maximum LST determined for each Rg class and by excluding Rg above a threshold which does not take into account the LST variation due to elevation effects (Fig. 5). The threshold of Rg is constrained as the maximum LST simulated by the third order polynomial, estimated by using the maximum LST value of each Rg class. Note that the number of class is estimated as 1% of the number of pixels.

4. Results and discussion

The three (EB, ML and DE) correction approaches are applied to ASTER LST data. As a first assessment of the performance of correction methods, the LST simulated by each model is compared to the ASTER LST and to the 1-cm depth soil temperature measurements. Then, the LST corrected by the EB method is qualitatively and quantitatively evaluated by visual inspection of the corrected images, statistical analyses of the spatial correlation between (uncorrected and corrected) LST and topography indicators, and the physical interpretation of the LST-fv feature space before and after correction .

4.1. Intercomparison and validation of LST models

4.1.1. Comparison between modeled and ASTER LST

The model-derived LST from the three methods are compared to the remotely sensed ASTER LST. The objective of this comparison is to examine the potential of EB method, compare to both ML and DE methods, to simulate LST

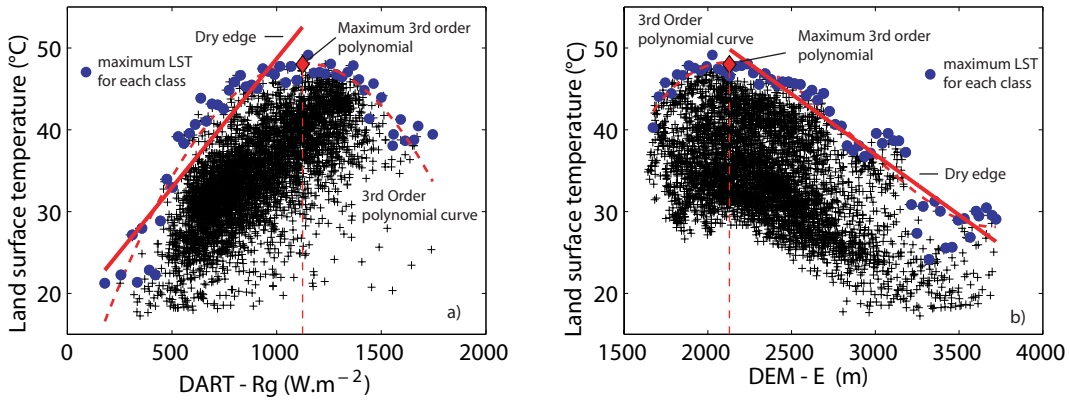

Figure 5: Example of the DE estimation (red lines) in a) LST-Rg space and b) LST-E space for September 5^{th}, 2014. Blue points correspond to the maximum temperature of each class. Red dashed curves are the 3^{rd} order polynomial curves of the maximum temperatures of each class. Red diamonds are the maximum temperatures of the 3^{rd} order polynomials that correspond to the thresholds for estimating DE

in a range of surface and topographic conditions by using pixel scale E and Rg. As LST is greatly controlled by topography effects over the study area, a high R value and a low RMSD value would indicate satisfactory results.

Fig. 6 plots simulated LST versus ASTER LST and Table 1 lists the correlation coefficient (R), bias, slope of linear regression (S) and RMSD between model-derived and ASTER LST for each of the three ASTER overpass dates separately. All biases are equal to zero due to the calibration procedure of the correction models using ASTER LST observations. Regarding the ML regression approach, Fig. 6 a,d,g and Table 1 shows satisfying results with an R of 0.76 and a RMSD of about 3.6°C. The statistical regularity obtained between the three dates reflects a certain robustness of the ML regression technique. Its performance can be explained by the relatively simple context of the study area including mostly wet vegetation at the valley bottom and mostly dry bare soil everywhere else. A poorer efficiency of the ML regression method would be expected in more heterogeneous conditions including the presence of vegetation on the slopes. Regarding the DE approach, Fig. 6 b,e,h indicate significant underestimation of LST estimates in the lower range of ASTER LST values and an overestimation in the higher range. Although the slope between model-derived LST and ASTER LST is generally close to 1, the RMSD (5.8°C) is significantly larger than for the ML case (see statistical results in Table 1) due to an overestimation of topographic effects by the DE correction method. In fact, the DE approach assumes that all pixels have the same sensitivity to topography as dry bare soil, although dry bare soil is much more affected by Rg than wet bare soil or vegetated surfaces. This is the reason why the LST simulated by the DE approach covers a larger range of values than ASTER LST (see Fig. 6). In fact, the main issue with this approach is the non representation of other conditions than dry bare soil, thus the need for taking into account the different behaviors of soil and vegetation components.

The statistics presented in Table 1 and the scatterplots in Fig. 6 c,f,i indicate that the dual-source EB model performs relatively better than the simpler ML and DE methods. The mean R and RMSD between model-derived and ASTER LST is 0.82 and 3°C, respectively. The consistency of the results obtained between the three dates reveals the robustness of the EB equations, as for the ML method. Moreover, the EB approach is able to retrieve a physically consistent temperature lapse rate based on ASTER and simulated LST (Table 2). The LR obtained through the minimization of the cost function in eq. 10, is close to the values found in the literature. Under standard atmospheric conditions the mean atmospheric LR is -6.4°C.km^{-1} (Glickman and Zenk, 2000). However it is affected by the moisture content of air: in dry condition, a LR of -10°C.km^{-1} is often used to calculate temperature changes (Glickman and Zenk, 2000) while in wet condition, the LR is close -5°C.km^{-1} in a saturated air. Regarding the values obtained here (Table 2), the 5^{th} September image has a LR of -8.9°C.km^{-1} near the LR in dry condition found in literature. This result is consistent with the fact that this date has the drier air condition (air humidity of 17%). Likewise, the image with the higher air humidity (30^{th} of April) has the lower LR estimated as -5.3°C.km^{-1}.

Regarding the dryness index of the surface soil (Table 2, fss) estimated by inversion of the soil EB, results illustrate a relatively dry soil (fss larger than 0.5) for the three dates as expected given the semi-arid climate of the

area . For example the retrieved fss is 0.95 on the 14^{th} April. Regarding the inverted vegetation water stress index (Table 2, fsv), dryness indices are generally close to 1. For example, the retrieved fsv is equal to 0.85 on the 30^{th} April. Although the vegetation in the stream valley is expected to be well-watered (i.e. not undergoing water stress) such results can be explained by the presence of sparse vegetation over the whole area. Such (potentially stressed) vegetation has a strong impact on the fsv inversion.

When analyzing the results obtained for each model, the EB approach gives generally the best statistical results in terms of R and RMSD between simulated and ASTER LST. In particular, the EB model is able to reproduce the spatial patterns of the LST estimated from ASTER with an R of 0.85 on the 5^{th} of September. The soil/vegetation partitioning and the physical representation of the nonlinear relationship between LST and Rg (as expressed by the net radiation of EB equations) both explain the superiority of the EB approach. (Table 1).

Table 1: Statistical results of the spatial comparison between simulated and ASTER LST for each model and each ASTER overpass date separately. The correlation coefficient (R), bias, slope of linear regression (S) and root mean square difference (RMSD) are listed. *LR*, fss and fsv are the environmental lapse rate, dryness index and vegetation water stress index, respectively.

date		ML	DE	EB
14/04/2014	R (-)	0.74	0.52	0.79
	bias (°C)	0	0	0
	S (-)	0.85	0.61	0.62
	RMSD (°C)	3.94	5.49	3.14
30/04/2014	R (-)	0.76	0.68	0.82
	bias (°C)	0	0	0
	S (-)	0.73	0.99	0.65
	RMSD (°C)	3.26	5.22	2.79
05/09/2014	R (-)	0.79	0.82	0.85
	bias (°C)	0	0	0
	S (-)	0.77	1.34	0.74
	RMSD (°C)	3.8	5.95	3.18

Table 2: *LR*, fss and fsv are the environmental lapse rate, dryness index and vegetation water stress index, respectively.

Date	fss	fsv	LR (°C.km^{-1})
14/04/2014	0.95	1	-5.9
30/04/2014	1	0.85	-5.3
05/09/2014	0.93	0.89	-8.9

4.1.2. Comparison between modeled LST and in situ soil temperature

The performance of the EB model is also assessed by comparing both the ASTER and simulated LST to the measured surface soil temperature (ibutton sensors). The EB model is implemented at both 8 m and 90 m resolution using the corresponding DEMs. The 90 m resolution LST is simulated as previously. The 8 m resolution LST is simulated by running the EB model using the LR, fss and fsv parameters retrieved from 90 m resolution ASTER data. Comparisons are made by extracting the LST pixels where temperature sensors are located.

The error statistics between LST and ground measurement are presented in Table 3 and scatterplots are displayed at Fig. 7. Note that the 14^{th} April has fewer points due to snow and clouds cover. When comparing the set of results, it is clear that the model-derived LST and ASTER LST give similar results in terms of both R and RMSD. For example, regarding the 30^{th} April, the simulated LST compares slightly better with ibutton measurements than with the ASTER LST. At the same (90 m) resolution, the EB simulation reduces the RMSD between LST and ibutton temperature by approximately 0.57°C. Regarding the bias, the obtained results are contrasted between the two first dates (bias is about 2.5°C) and the 5^{th} of September (bias is approaching the accuracy limit of the ibutton sensors; this is a limitation of using low cost temperature sensors). This could be due to the soil thermal inertia capacity since ibutton measurements

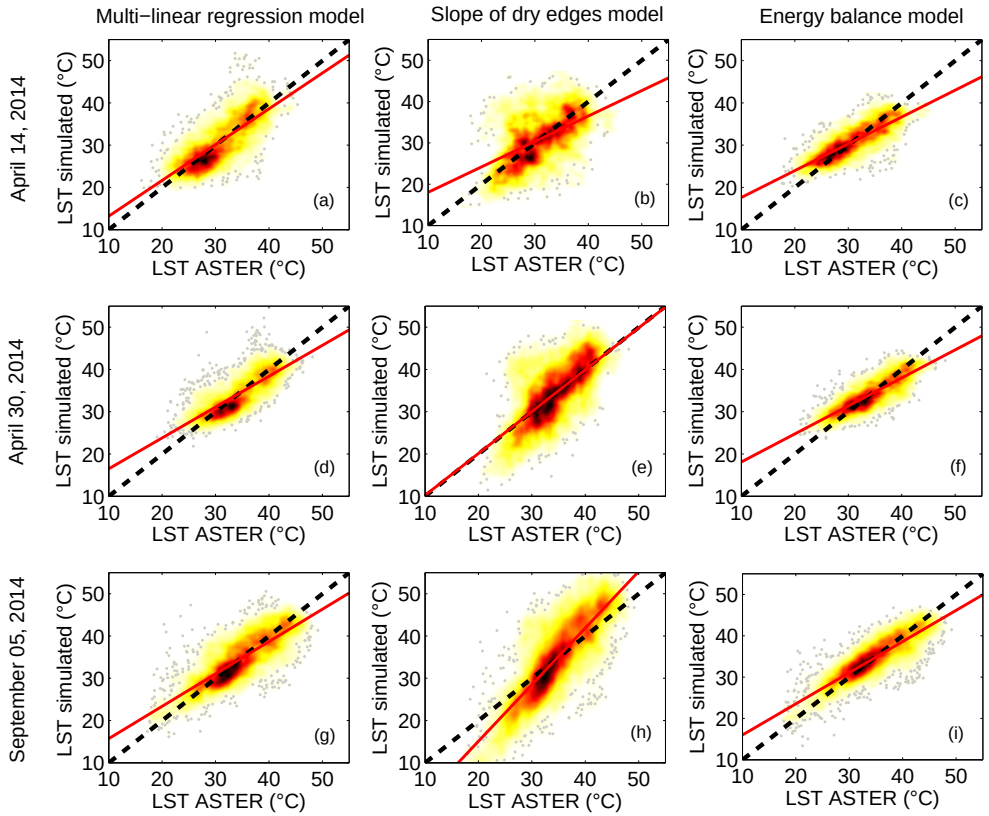

Figure 6: Scatterplots of simulated LST versus ASTER LST for the three dates and for the ML (left), DE (middle) and EB (right column) models separately. Red lines represent the slope of linear regression. Dashed lines represent the 1:1 line.

are made at a 1 cm depth whereas the simulated LST is the skin surface temperature. For example, the two first dates (14^{th} and 30^{th} April) have a positive bias, which means that the mean ibutton temperature is about 3°C colder than the remotely sensed LST. This phenomenon could be explained by the rapid morning heating of the immediate surface after a cold night. The air temperature before sunrise was 10°C and 8°C for the 14^{th} and 30^{th} of April, respectively. This characteristic is less noticeable for the 5^{th} of September because on that date, the air temperature is less variable between day and night . Higher temperatures (22.3°C before sunrise) were indeed recorded during the night before with a diurnal temperature variation of ~5°C.

Fig. 7 plots ASTER and simulated LST versus ibutton measurements and Table 3 lists the R, bias and RMSD between model-derived and ASTER LST versus ibutton measurements for each of the three ASTER overpass dates separately. Results indicate that the LST simulated for the warmer pixels are systematically lower than remotely sensed LST. This could be explained by the static (instantaneous) nature of the EB model, as the LST is simulated at a specific instant and, thus neglecting the heat storage. By contrast, ASTER provides information about the real state of the surface skin, which is potentially affected by the heat accumulation over the slopes that have been exposed to the sun for a period of time prior to the ASTER overpass.

The improvement between the LST simulated at 90 m and 8 m resolution are not as great as expected due to the topography variability around ibutton sensors. Actually, the ibuttons were set up in a topographic environment that was relatively homogeneous at the 90 m scale, given that the primary objective of the study was to correct topographic effects at the ASTER resolution. In consequence, the LSTs simulated at 90 m and 8 m resolution compare similarly with the 1-cm depth soil temperature measurements.

Table 3: Statistics of the comparison between ASTER or simulated LST and the 1-cm depth soil temperature measurements by the ibutton sensors. The correlation coefficient (R), bias, root mean square difference (RMSD) and standard deviation (σ) are listed. (-) means dimensionless unit.

date		ASTER	Model 90 m	Model 8 m
14/04/2014	σ (°C)	7.31	4.20	3.57
	R (-)	0.64	0.75	0.68
	bias (°C)	3.04	1.48	3.41
	RMSD (°C)	6.28	3.41	3.53
30/04/2014	σ (°C)	6.05	4.11	3.90
	R (-)	0.68	0.68	0.70
	bias (°C)	3.38	2.74	2.74
	RMSD (°C)	5.98	5.41	5.32
05/09/2014	σ (°C)	6.22	4.74	5.06
	R (-)	0.67	0.64	0.65
	bias (°C)	0.78	-0.43	-0.91
	RMSD (°C)	5.31	5.19	5.22

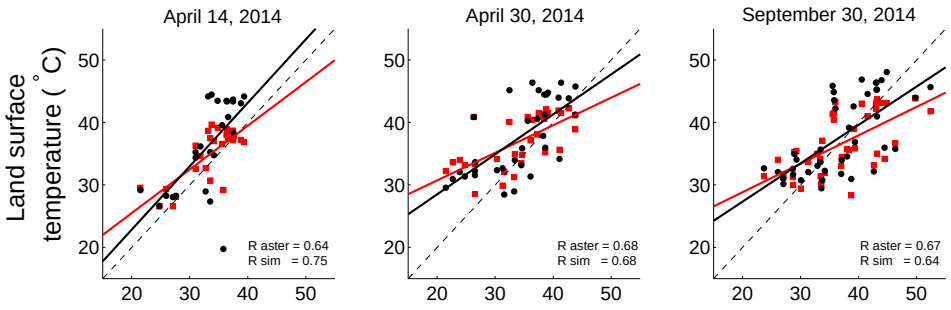

Figure 7: Scatterplots of ASTER and simulated LST at 90m resolution versus ibutton measurements for each ASTER overpass date, separately. Red squares are simulated LST and black dots are ASTER LST. Red lines represent the slope of linear regression for simulated LST and black lines represent the slope of linear regression for ASTER LST. Dashed lines represent the 1:1 line.

4.2. *Assessment of LST topographic correction*

In order to evaluate the performance of the topographic correction method based on the dual-source EB equations, the LST data before and after correction are analyzed. The visual inspection of LST images and the interpretation of the LST-fv feature space before and after correction can help assess the goodness of the correction . If the correction is efficient, temperature difference between sun and shadow exposed slopes should be reduced. Temperature at high elevation should also be reduced. Nevertheless, vegetation and soil moisture should be still apparent.

Visual comparisons of the images before and after topographic correction shown in Fig. 8 suggest that the topographic effects are much reduced after correction . The black patches in the images for April 14^{th} and 30^{th} correspond to snow cover and clouds. The remaining temperature differences after correction for elevation effects are expected to be small. Indeed, these differences should be related to vegetation and soil moisture conditions only and those conditions are quite homogeneous in the study area apart from some localized spots in the valley. Interestingly enough, the ridgeline (located at the top left of the scene) is still conspicuous after correction . This under-correction of ridgelines is probably attributed to a problem with the or ASTER data geo-referencing, as a pixel shift could affect results. (Nuth and Kääb, 2011).

In Fig. 8, the sun facing slope on the top left of the scene is still noticeable certainly as a result of the underestimation of LST simulated over this area. As mentioned in the previous section, this effect could be due to the soil thermal inertia capacity, which is not taken into account by the instantaneous EB model.

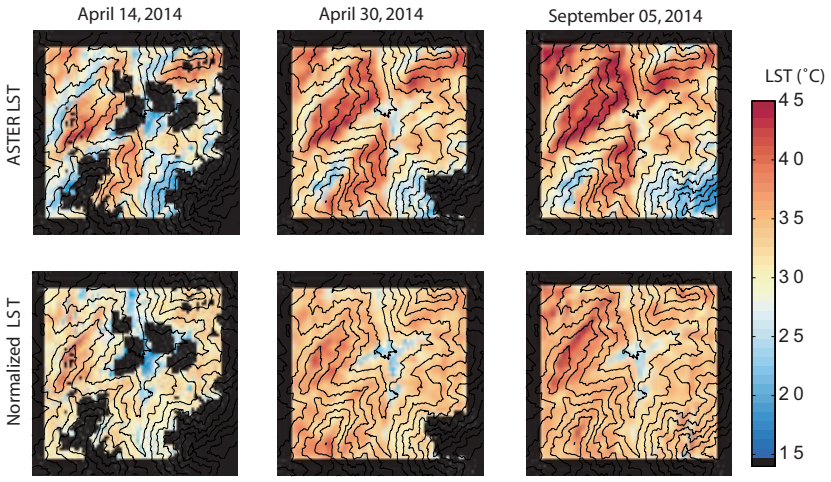

Figure 8: Images of the LST observed by ASTER before (up) and after (down) correction for topographic effects on the three ASTER overpass dates separately. Black lines represent the elevation contour lines between 1800 and 3600 m with a 200 m increment.

According to Reeder (2002), a successful topographic correction should remove or greatly reduce the correlation between LST and the topographic variables, especially the solar radiation (Zhang and Gao, 2011). As shown in Table 4, strong correlations are found between LST and Rg over rugged terrain before correction . The correlation coefficients after topographic correction are greatly reduced (from 0.76 to 0.11 for the April 30^{th}, for example) consistent with the study in Reeder (2002). Negative correlations are obtained on the 14^{th} of April and the 05^{th} of September. This could be due to the artifact observed over the ridge line, which is particularly visible on those dates (see Fig. 8) or a coregistration error between DEM and the LST images.

As an additional assessment of the correction performance, we compare the LST-fv space patterns before and after correction. As topographic correction aims at removing the topographic influence by deriving the LST that would be observed in a flat terrain, the LST-fv feature space after correction should be similar to the LST-fv feature spaces classically observed in flat conditions. In flat terrain all LST pixels are contained in the polygon defined by the temperature endmembers corresponding to fully dry and wet conditions for both soil/vegetation components (Fig. 9). The four temperature endmembers (T_s, dry, T_v, dry, T_s, wet and T_v, wet) were simulated by the EB equations using the average of $E(\langle E \rangle)$ and $Rg(\langle Rg \rangle)$ at the image scale. In practice, the LST-fv space was defined in a two step procedure. First, the temperature endmembers were estimated from EB equations and were located within the space defined by

Table 4: Correlation coefficient (R) between Rg and LST before and after topographic normalization on the three ASTER overpass dates separately.

	R between Rg and LST		
	14/04/2014	30/04/2014	05/09/2014
before normalization	0.75	0.76	0.67
after normalization	-0.05	0.11	-0.11

LST and fv (Long and Singh, 2012; Merlin, 2013). Then, the vertices of the obtained polygons were connected by straight lines (Moran et al., 1994) to interpolate the dry and wet boundaries over the full range of vegetation cover. The analysis of the LST-fv space after correction (Fig. 9) exhibits a distribution similar to that typically obtained in flat region (e.g. Stefan et al. (2015)). Specifically the topographic correction method has removed or greatly reduced the number of pixels outside the LST-fv space meaning above or below the dry and wet edges. An interesting feature is that the pixels that remain outside the polygon (above the dry edge) after correction systematically correspond to pixels located near the ridge lines. Such results are fully consistent with the previous comparison between the simulated LST and 1 cm depth soil temperature measurements.

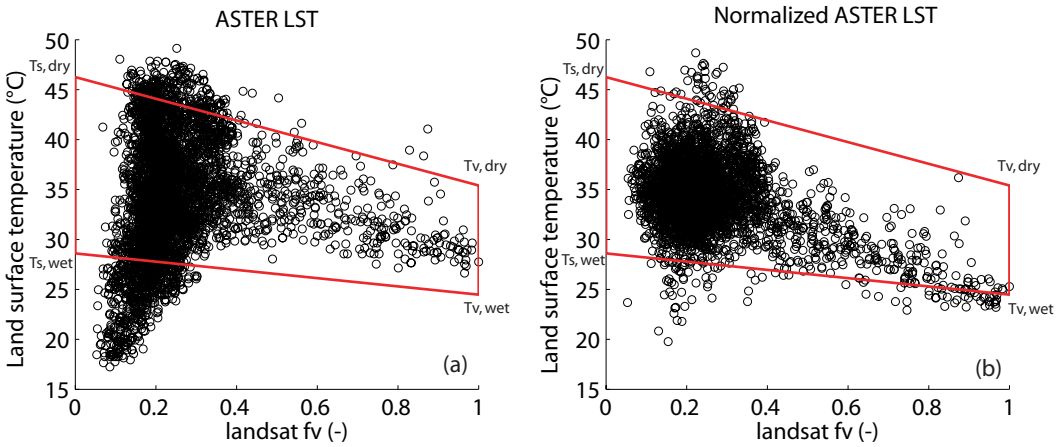

Figure 9: The LST-fv feature space is plotted on September the 5th before (a) and after (b) topographic correction .

5. Summary and conclusion

This paper develops a physically-based method to correct the satellite-derived land surface temperature (LST) for topography-induced variations of solar radiation and air temperature over mountainous areas. Both topographic effects on LST are first quantified by inverting a dual-source soil/vegetation energy balance (EB) model forced by 1) the solar radiation (Rg) simulated by DART model that uses a DEM as input, 2) a satellite-derived vegetation index fv, and 3) meteorological data available at a given location. The topographic correction model is calibrated in two main steps using ASTER LST observations. The first step removes any possible bias in modeled LST. The second step adjusts environmental lapse rate (LR), surface soil dryness index (fss) and vegetation water stress index (fsv) by minimizing the RMSD between ASTER LST and model-derived LST, for each ASTER overpass date separately. Once the LST model has been calibrated, it can be applied to any spatial resolution, provided a DEM is available at the target resolution. Satellite LST is then corrected for topography by subtracting the simulated illumination (DART-simulated solar radiation) and elevation (LR-derived air temperature) effects. The approach is tested on three ASTER overpass dates over a 6 km by 6 km area in the Atlas Mountain (Morocco): April 14^{th}, April 30^{th} and September 05^{th}, 2014.

For this rugged test site, the mean correlation coefficient and RMSD between EB-simulated and ASTER LST are estimated as 0.80 and 3°C , respectively. The EB-based approach is more accurate in terms of LST estimates than

the multi-linear (ML) regression based on DART solar radiation and elevation data. It is also more accurate than a semi-empirical model built from the dry edge of the LST-illumination and LST-elevation feature spaces. Such results are explained by the fact that the EB model explicitly represents both soil and vegetation components, whose surface fluxes are very differently affected by topography. Moreover, the EB approach is able to physically represent the nonlinearity between LST and Rg via the net radiation component. As a further advantage of the physically-based method, the EB equation can be used to retrieve the LR at the time of ASTER overpass. It is important to note that the obtained LR is close to the values found in the literature, with a LR of -8.9°C.km^{-1} (5^{th} of September) in dry air condition; while a LR of -5.3°C.km^{-1} has been estimated for the 30^{th} of April corresponding to the highest observed relative air humidity.

The LST simulated by the EB approach is also evaluated against an extensive ground dataset of 135 autonomous 1-cm depth temperature sensors deployed over the steep-sided study area. The EB model is applied to both 8 m and 90 m resolution DEMs. While the mean RMSD between 90 m resolution ASTER LST and ibutton measurements is 6.1°C, the RMSD between EB LST and localized ibutton measurements is 5.4 and 5.3 °C for a DEM at 90 m and 8 m resolution, respectively. Last, the topography-corrected ASTER LST is analyzed both qualitatively and quantitatively. The visual comparison before and after correction suggests that the topography-induced variations of solar radiation and air temperature are a much reduced impact on LST after correction. Especially, the LST spatial distribution is similar to that typically observed over a flat area where the solar radiation reaching the surface can be considered uniform. Moreover, the LST-fv feature space after correction is similar to the LST-fv feature space classically observed in flat conditions. Quantitatively, the strong correlations found between LST and Rg over rugged terrain before correction are greatly reduced after topographic correction (from 0.76 to 0.11 for the April 30^{th}).

For the first time, a correction method for topography-induced variations of solar radiation and air temperature has been applied to satellite LST. While LST data are widely used over relatively flat areas, this new approach offers the opportunity for new applications over mountainous areas. such a correction method could potentially be used in conjunction with LST-based evapotranspiration methods over agricultural (Merlin et al., 2010b; Mattar et al., 2014) and complex terrain (Olivera-Guerra et al., 2014), soil moisture disaggregation methods (Merlin et al., 2012; Malbéteau et al., 2016) and forest fire prediction models (Leblon, 2005), among others. Note that the operational utility of the EB correction method over wide areas relies on the availability of ancillary data composed of meteorological forcing. Moreover, Integrating heat storage variation in a dynamic version of the EB model (Danilina et al., 2012) would improve the simulation of LST over the slopes exposed to the sun prior to the satellite overpass. Such developments could be fostered by the future availability of LST data at high spatial and temporal resolution (Wu et al., 2015).

Acknowledgements

This study was carried out within the frame of the Joint International Laboratory TREMA http://trema.ucam.ac.ma and was supported by the MIXMOD-E project (ANR-13-JS06-0003-01) funded by the French agency ANR (Agence Nationale de la Recherche) and the REC project (RISE-2014-645642- REC) funded by the European H2020 program. The acquisition of the Pliades images was supported by the CNES through the ISIS program. Mohamed Kasbani,participant of the experiment, is gratefully acknowledged.

References

Abrams, M., 2000. The Advanced Spaceborne Thermal Emission and Reflection Radiometer (ASTER): Data products for the high spatial resolution imager on NASA's Terra platform. International Journal of Remote Sensing 21 (5), 847–859.

Allen, R. G., Pereira, L. S., Raes, D., Smith, M., 1998. Crop evapotranspiration- guidelines fo computing crop water requirements. FAO Irrigation and Drainage Paper 56, 1–15.

Allen, R. G., Tasumi, M., Morse, A., Trezza, R., Wright, J. L., Bastiaanssen, W., Kramber, W., Lorite, I., Robison, C. W., Morse, A., Trezza, R., Wright, J. L., Bastiaanssen, W., Kramber, W., Lorite, I., Robison, C. W., Morse, A., Trezza, R., Wright, J. L., Bastiaanssen, W., Kramber, W., Lorite, I., Robison, C. W., 2007. Satellite-Based Energy Balance for Mapping Evapotranspiration with Internalized Calibration (METRIC)Applications. Journal of Irrigation and Drainage Engineering 133 (4), 395–406.

Allen, R. G., Trezza, R., Tasumi, M., 2006. Analytical integrated functions for daily solar radiation on slopes. Agricultural and Forest Meteorology 139 (1-2), 55–73.

Anderson, M. C., Norman, J. M., Kustas, W., Houborg, R., Starks, P., Agam, N., dec 2008. A thermal-based remote sensing technique for routine mapping of land-surface carbon, water and energy fluxes from field to regional scales. Remote Sensing of Environment 112 (12), 4227–4241.

Bastiaanssen, W., Menenti, M., Feddes, R., Holtslag, A., 1998. A remote sensing surface energy balance algorithm for land (SEBAL). 1. Formulation. Journal of Hydrology 212-213, 198–212.

Berthier, E., Vincent, C., Magnússon, E., Gunnlaugsson, Á. ., Pitte, P., Le Meur, E., Masiokas, M., Ruiz, L., Pálsson, F., Belart, J. M. C., Wagnon, P., dec 2014. Glacier topography and elevation changes derived from Pléiades sub-meter stereo images. The Cryosphere 8 (6), 2275–2291.

Bertoldi, G., Notarnicola, C., Leitinger, G., Endrizzi, S., Zebisch, M., Della Chiesa, S., Tappeiner, U., 2010. Topographical and ecohydrological controls on land surface temperature in an alpine catchment. Ecohydrology 3, 189–204.

Boulet, G., Chehbouni, A., Gentine, P., Duchemin, B., Ezzahar, J., Hadria, R., 2007. Monitoring water stress using time series of observed to unstressed surface temperature difference. Agricultural and Forest Meteorology 146 (3-4), 159–172.

Bristow, K. L., jan 1987. On solving the surface energy balance equation for surface temperature. Agricultural and Forest Meteorology 39 (1), 49–54.

Brunsell, N. a., Gillies, R. R., dec 2003. Length Scale Analysis of Surface Energy Fluxes Derived from Remote Sensing. Journal of Hydrometeorology 4 (6), 1212–1219.

Brutsaert, W., oct 1975. On a derivable formula for long-wave radiation from clear skies. Water Resources Research 11 (5), 742–744.

Cammalleri, C., Vogt, J., 2015. On the Role of Land Surface Temperature as Proxy of Soil Moisture Status for Drought Monitoring in Europe. Remote Sensing 7 (12), 16849–16864.

Chehbouni, A., Escadafal, R., Duchemin, B., Boulet, G., Simonneaux, V., Dedieu, G., Mougenot, B., Khabba, S., Kharrou, H., Maisongrande, P., Merlin, O., Chaponnière, A., Ezzahar, J., ErRaki, S., Hoedjes, J., Hadria, R., Abourida, A., Cheggour, A., Raibi, F., Boudhar, A., Benhadj, I., Hanich, L., Benkaddour, A., Guemouria, N., Chehbouni, A. H., Lahrouni, A., Olioso, A., Jacob, F., Williams, D. G., Sobrino, J. A., 2008. An integrated modelling and remote sensing approach for hydrological study in arid and semiarid regions: the SUDMED Programme. International Journal of Remote Sensing 29 (17-18), 5161–5181.

Choudhury, B., Reginato, R., Idso, S., may 1986. An analysis of infrared temperature observations over wheat and calculation of latent heat flux. Agricultural and Forest Meteorology 37 (1), 75–88.

Claverie, M., Vermote, E. F., Franch, B., Masek, J. G., 2015. Evaluation of the Landsat-5 TM and Landsat-7 ETM+ surface reflectance products. Remote Sensing of Environment 169, 390–403.

Coret, L., Briottet, X., Kerr, Y., Chehbouni, A., 2004. Simulation Study of View Angle Effects on Thermal Infrared Measurements Over Heterogeneous Surfaces. IEEE Transactions on Geoscience and Remote Sensing 42 (3), 664–672.

Danilina, I., Gillespie, A. R., Balick, L., Mushkin, A., Smith, M., Blumberg, D., 2013. Compensation for subpixel roughness effects in thermal infrared images. International Journal of Remote Sensing 34 (9-10), 3425–3436.

Danilina, I., Gillespie, A. R., Balick, L. K., Mushkin, A., O'Neal, M. A., 2012. Performance of a thermal-infrared radiosity and heat-diffusion model for estimating sub-pixel radiant temperatures over the course of a day. Remote Sensing of Environment 124, 492–501.

Dozier, J., 1980. A Clear-Sky Spectral Solar Radiation Model. Water Resources Research 16 (4), 709–718.

Dozier, J., Outcalt, S. I., 1979. An Approach toward Energy Balance Simulation over Rugged Terrain. Geographical Analysis 11 (1), 65–85.

Dubayah, R., sep 1992. Estimating net solar radiation using Landsat Thematic Mapper and digital elevation data. Water Resources Research 28 (9), 2469–2484.

Dubayah, R. C., 1994. Modeling a solar radiation topoclimatology for the Rio Grande River Basin. Journal of Vegetation Science 5 (5), 627–640.

Eckmann, T. C., Roberts, D. A., Still, C. J., 2008. Using multiple endmember spectral mixture analysis to retrieve subpixel fire properties from MODIS. Remote Sensing of Environment 112 (10), 3773–3783.

Endrizzi, S., Gruber, S., Amico, M. D., Rigon, R., 2013. GEOtop 2 . 0 : simulating the combined energy and water balance at and below the land surface accounting for soil freezing , snow cover and terrain e ff ects. Geosci. Model Dev. Discuss. (ii), 6279–6341.

Essery, R., Marks, D., 2007. Scaling and parametrization of clear-sky solar radiation over complex topography. Journal of Geophysical Research: Atmospheres 112 (10), 1–12.

Garen, D. C., Marks, D., 2005. Spatially distributed energy balance snowmelt modelling in a mountainous river basin: Estimation of meteorological inputs and verification of model results. Journal of Hydrology 315, 126–153.

Gastellu-Etchegorry, J. P., 2008. 3D modeling of satellite spectral images, radiation budget and energy budget of urban landscapes. Meteorology and Atmospheric Physics 102 (3-4), 187–207.

Gastellu-Etchegorry, J. P., Demarez, V., Pinel, V., Zagolski, F., 1996. Modeling radiative transfer in heterogeneous 3-D vegetation canopies. Remote Sensing of Environment 58 (November 1995), 131–156.

Gastellu-Etchegorry, J. P., Martin, E., Gascon, F., jan 2004. DART: a 3D model for simulating satellite images and studying surface radiation budget. International Journal of Remote Sensing 25 (1), 73–96.

Gillespie, A., Rokugawa, S., Matsunaga, T., Steven Cothern, J., Hook, S., Kahle, A. B., 1998. A temperature and emissivity separation algorithm for advanced spaceborne thermal emission and reflection radiometer (ASTER) images. IEEE Transactions on Geoscience and Remote Sensing 36 (4), 1113–1126.

Glickman, T. S., Zenk, W., 2000. Glossary of Meteorology (2nd ed.). American Meteorological Society, Boston.

Goward, S. N., Cruickshanks, G. D., Hope, A. S., 1985. Observed relation between thermal emission and reflected spectral radiance of a complex vegetated landscape. Remote Sensing of Environment 18 (2), 137–146.

Guillevic, P., Gastellu-Etchegorry, J.-P., Demarty, J., Prévot, L., 2003. Thermal infrared radiative transfer within three-dimensional vegetation covers. Journal of Geophysical Research 108 (D8), 4248.

Gutman, G., Ignatov, A., 1998. The derivation of the green vegetation fraction from NOAA/AVHRR data for use in numerical weather prediction models. International Journal of Remote Sensing 19 (8), 1533–1543.

Hais, M., Kučera, T., nov 2009. The influence of topography on the forest surface temperature retrieved from Landsat TM, ETM + and ASTER thermal channels. ISPRS Journal of Photogrammetry and Remote Sensing 64 (6), 585–591.

Hall, F. G., Huemmrich, K. F., Goetz, S. J., Sellers, P. J., Nickeson, J. E., 1992. Satellite remote sensing of surface energy balance: Success, failures, and unresolved issues in FIFE. Journal of Geophysical Research: Atmospheres 97 (D17), 19061–19089.

Hansen, J., Ruedy, R., Sato, M., Lo, K., 2010. Global surface temperature change. Rev. Geophys. 48 (4), RG4004.

Herrero, J., Polo, M. J., 2012. Parameterization of atmospheric longwave emissivity in a mountainous site for all sky conditions. Hydrology and

Earth System Sciences 16 (9), 3139–3147.
Hubbart, J., Link, T., Campbell, C., Cobos, D., 2005. Evaluation of a low-cost temperature measurement system for environmental applications. Hydrological Processes 19 (7), 1517–1523.
Iziomon, M. G., Mayer, H., Matzarakis, A., 2003. Downward atmospheric longwave irradiance under clear and cloudy skies: Measurement and parameterization. Journal of Atmospheric and Solar-Terrestrial Physics 65 (10), 1107–1116.
Jarlan, L., Khabba, S., Er-Raki, S., Le Page, M., Hanich, L., Fakir, Y., Merlin, O., Mangiarotti, S., Gascoin, S., Ezzahar, J., Kharrou, M., Berjamy, B., Saaïdi, A., Boudhar, A., Benkaddour, A., Laftouhi, N., Abaoui, J., Tavernier, A., Boulet, G., Simonneaux, V., Driouech, F., El Adnani, M., El Fazziki, A., Amenzou, N., Raibi, F., El Mandour, A., Ibouh, H., Le Dantec, V., Habets, F., Tramblay, Y., Mougenot, B., Leblanc, M., El Faïz, M., Drapeau, L., Coudert, B., Hagolle, O., Filali, N., Belaqziz, S., Marchane, A., Szczypta, C., Toumi, J., Diarra, A., Aouade, G., Hajhouji, Y., Nassah, H., Bigeard, G., Chirouze, J., Boukhari, K., Abourida, A., Richard, B., Fanise, P., Kasbani, M., Chakir, A., Zribi, M., Marah, H., Naimi, A., Mokssit, A., Kerr, Y., Escadafal, R., oct 2015. Remote Sensing of Water Resources in Semi-Arid Mediterranean Areas: the joint international laboratory TREMA. International Journal of Remote Sensing 36 (19-20), 4879–4917.
Julien, Y., Sobrino, J. a., feb 2009. The Yearly Land Cover Dynamics (YLCD) method: An analysis of global vegetation from NDVI and LST parameters. Remote Sensing of Environment 113 (2), 329–334.
Karnieli, A., Agam, N., Pinker, R. T., Anderson, M., Imhoff, M. L., Gutman, G. G., Panov, N., Goldberg, A., feb 2010. Use of NDVI and Land Surface Temperature for Drought Assessment: Merits and Limitations. Journal of Climate 23 (3), 618–633.
Kim, J., Hogue, T. S., feb 2012. Improving Spatial Soil Moisture Representation Through Integration of AMSR-E and MODIS Products. IEEE Transactions on Geoscience and Remote Sensing 50 (2), 446–460.
Kogan, F. N., 2001. Operational space technology for global vegetation assessment. Bulletin of the American Meteorological Society 82 (9), 1949–1964.
Kustas, W., Anderson, M., dec 2009. Advances in thermal infrared remote sensing for land surface modeling. Agricultural and Forest Meteorology 149 (12), 2071–2081.
Kustas, W. P., Daughtry, C. S., feb 1990. Estimation of the soil heat flux/net radiation ratio from spectral data. Agricultural and Forest Meteorology 49 (3), 205–223.
Kustas, W. P., Rango, A., Uijlenhoet, R., 1994. A simple energy budget algorithm for the snowmelt runoff model. Water Resources Research 30 (5), 1515–1527.
Lagouarde, J. P., Kerr, Y. H., Brunet, Y., 1995. An experimental study of angular effects on surface temperature for various plant canopies and bare soils. Agricultural and Forest Meteorology 77 (3-4), 167–190.
Leblon, B., 2005. Monitoring forest fire danger with remote sensing. Natural Hazards 35 (3), 343–359.
Li, F., Jackson, T. J., Kustas, P., Schmugge, T. J., French, A. N., Cosh, H., Bindlish, R., 2004. Deriving land surface temperature from Landsat 5 and 7 during Smacex/Smex. Remote Sensing of Environment 92 (4), 521 – 534.
Liu, Y., Hiyama, T., Yamaguchi, Y., nov 2006. Scaling of land surface temperature using satellite data: A case examination on ASTER and MODIS products over a heterogeneous terrain area. Remote Sensing of Environment 105 (2), 115–128.
Liu, Y., Noumi, Y., Yamaguchi, Y., 2009. Discrepancy between ASTER- and MODIS- derived land surface temperatures: Terrain effects. Sensors 9 (2), 1054–1066.
Long, D., Singh, V. P., jun 2012. A Two-source Trapezoid Model for Evapotranspiration (TTME) from satellite imagery. Remote Sensing of Environment 121, 370–388.
Malbéteau, Y., Merlin, O., Molero, B., Rüdiger, C., Bacon, S., mar 2016. DisPATCh as a tool to evaluate coarse-scale remotely sensed soil moisture using localized in situ measurements: Application to SMOS and AMSR-E data in Southeastern Australia. International Journal of Applied Earth Observation and Geoinformation 45, 221–234.
Marti, R., Gascoin, S., Houet, T., Laffly, D., René, P., 2014. Evaluation du modèle numérique d'élévation d'une petit glacier de montagne généré à partir d'images stéréoscopiques Pléiades. cas du glacier d'Ossoue, Pyrénées françaises. Revue Française de Photogrammétrie et de Télédétection 208, 57–62.
Mattar, C., Franch, B., Sobrino, J. a., Corbari, C., Jiménez-Muñoz, J. C., Olivera-Guerra, L., Skokovic, D., Sória, G., Oltra-Carriò, R., Julien, Y., Mancini, M., 2014. Impacts of the broadband albedo on actual evapotranspiration estimated by S-SEBI model over an agricultural area. Remote Sensing of Environment 147, 23–42.
Menenti, M., Bastiaanssen, W., van Eick, D., Abd el Karim, M., jan 1989. Linear relationships between surface reflectance and temperature and their application to map actual evaporation of groundwater. Advances in Space Research 9 (1), 165–176.
Merlin, O., 2013. An original interpretation of the wet edge of the surface temperaturealbedo space to estimate crop evapotranspiration (SEB-1S), and its validation over an irrigated area in northwestern Mexico. Hydrology and Earth System Sciences 17 (9), 3623–3637.
Merlin, O., Al Bitar, A., Walker, J. P., Kerr, Y., oct 2010a. An improved algorithm for disaggregating microwave-derived soil moisture based on red, near-infrared and thermal-infrared data. Remote Sensing of Environment 114 (10), 2305–2316.
Merlin, O., Chehbouni, A., jan 2004. Different approaches in estimating heat flux using dual angle observations of radiative surface temperature. International Journal of Remote Sensing 25 (1), 275–289.
Merlin, O., Chehbouni, A., Kerr, Y., Njoku, E., Entekhabi, D., sep 2005. A combined modeling and multispectral/multiresolution remote sensing approach for disaggregation of surface soil moisture: application to SMOS configuration. IEEE Transactions on Geoscience and Remote Sensing 43 (9), 2036–2050.
Merlin, O., Duchemin, B., Hagolle, O., Jacob, F., Coudert, B., Chehbouni, G., Dedieu, G., Garatuza, J., Kerr, Y., nov 2010b. Disaggregation of MODIS surface temperature over an agricultural area using a time series of Formosat-2 images. Remote Sensing of Environment 114 (11), 2500–2512.
Merlin, O., Rudiger, C., Al Bitar, A., Richaume, P., Walker, J. P., Kerr, Y. H., may 2012. Disaggregation of SMOS Soil Moisture in Southeastern Australia. IEEE Transactions on Geoscience and Remote Sensing 50 (5), 1556–1571.
Merlin, O., Walker, J., Chehbouni, A., Kerr, Y., oct 2008. Towards deterministic downscaling of SMOS soil moisture using MODIS derived soil evaporative efficiency. Remote Sensing of Environment 112 (10), 3935–3946.
Meybeck, M., Green, P., Vörösmarty, C., 2001. A New Typology for Mountains and Other Relief Classes. Mountain Research and Development

21 (1), 34–45.
Meyer, D., 2011. ASTER Global Digital Elevation Model Version 2 Summary of Validation Results. Japan Space Systems, 7.
Minnis, P., Khaiyer, M. M., 2000. Anisotropy of Land Surface Skin Temperature Derived from Satellite Data. Journal of Applied Meteorology 39 (7), 1117–1129.
Moran, M. S., Clarke, T. R., Inoue, Y., Vidal, A., 1994. Estimating crop water deficit using the relation between surface-air temperature and spectral vegetation index.
Nemani, R. R., Running, S. W., 1989. Estimation of regional surface resistance to evapotranspiration from NDVI and thermal-IR AVHRR data. [Normalized Difference Vegetation Index. Journal of Applied Meteorology 28, 276–284.
Norman, J. M., Divakarla, M., Goel, N. S., 1995. Algorithms for extracting information from remote thermal-IR observations of the earth's surface. Remote Sensing of Environment 51 (1), 157–168.
Nuth, C., Kääb, 2011. Co-registration and bias corrections of satellite elevation data sets for quantifying glacier thickness change. Cryosphere 5 (1), 271–290.
Olivera-Guerra, L., Mattar, C., Galleguillos, M., 2014. Estimation of real evapotranspiration and its variation in Mediterranean landscapes of central-southern Chile. International Journal of Applied Earth Observation and Geoinformation 28 (1), 160–169.
Peres, L. F., DaCamara, C. C., 2004. Land surface temperature and emissivity estimation based on the two-temperature method : sensitivity analysis using simulated MSG / SEVIRI data. Remote Sensing of Environment 91 (3-4), 377–389.
Prata, A. J., Caselles, V., Coll, C., Sobrino, J. A., Ottle, C., 1995. Thermal remote sensing of land surface temperature from satellites: Current status and future prospects. Remote Sensing Reviews 12 (3-4), 175–224.
Proy, C., Tanre, D., Deschamps, P., 1989. Evaluation of topographic effects in remotely sensed data. Remote Sensing of Environment 30 (1), 21–32.
Rasmussen, M. O., Pinheiro, A. C., Proud, S. R., Sandholt, I., 2010. Modeling angular dependences in land surface temperatures from the SEVIRI instrument onboard the geostationary meteosat second generation satellites. IEEE Transactions on Geoscience and Remote Sensing 48 (8), 3123–3133.
Raz-Yaseef, N., Rotenberg, E., Yakir, D., 2010. Effects of spatial variations in soil evaporation caused by tree shading on water flux partitioning in a semi-arid pine forest. Agricultural and Forest Meteorology 150 (3), 454–462.
Reeder, D. H., 2002. Topographic Correction of Satellite Images: Theory and Application.
Rigon, R., Bertoldi, G., Over, T. M., 2006. GEOtop: A Distributed Hydrological Model with Coupled Water and Energy Budgets. Journal of Hydrometeorology 7 (3), 371–388.
Rubio, E., Caselles, V., Coll, C., Valour, E., Sospedra, F., jan 2003. Thermalinfrared emissivities of natural surfaces: improvements on the experimental set-up and new measurements. International Journal of Remote Sensing 24 (24), 5379–5390.
Sandholt, I., Rasmussen, K., Andersen, J., feb 2002. A simple interpretation of the surface temperature/vegetation index space for assessment of surface moisture status. Remote Sensing of Environment 79 (2-3), 213–224.
Schmetz, J., Pili, P., Tjemkes, S., Just, D., Kerkmann, J., Rota, S., Ratier, A., 2002. Supplement to an introduction to Meteosat Second Generation (MSG) SEVIRI calibration. Bulletin of the American Meteorological Society 83 (7), 992.
Sepulcre-Cantó, G., Zarco-Tejada, P. J., Sobrino, J. a., Berni, J. a. J., Jiménez-Muñoz, J. C., Gastellu-Etchegorry, J. P., 2009. Discriminating irrigated and rainfed olive orchards with thermal ASTER imagery and DART 3D simulation. Agricultural and Forest Meteorology 149 (6-7), 962–975.
Shreve, F., apr 1924. Soil Temperature as Influenced by Altitude and Slope Exposure. Ecology 5 (2), 128–136.
Sobrino, J., Franch, B., Mattar, C., Jiménez-Muñoz, J., Corbari, C., 2012. A method to estimate soil moisture from Airborne Hyperspectral Scanner (AHS) and ASTER data: Application to SEN2FLEX and SEN3EXP campaigns. Remote Sensing of Environment 117, 415–428.
Sobrino, J. A., Cuenca, J., 1999. Angular variation of thermal infrared emissivity for some natural surfaces from experimental measurements. Appl. Opt. 38 (18), 3931–3936.
Sobrino, J. a., Mattar, C., Gastellu-Etchegorry, J. P., Jiménez-Muñoz, J. C., Grau, E., nov 2011. Evaluation of the DART 3D model in the thermal domain using satellite/airborne imagery and ground-based measurements. International Journal of Remote Sensing 32 (22), 7453–7477.
Stefan, V., Merlin, O., Er-Raki, S., Escorihuela, M.-j., Khabba, S., aug 2015. Consistency between In Situ, Model-Derived and High-Resolution-Image-Based Soil Temperature Endmembers: Towards a Robust Data-Based Model for Multi-Resolution Monitoring of Crop Evapotranspiration. Remote Sensing 7 (8), 10444–10479.
Susong, D., Marks, D., Garen, D., 1999. Methods for developing time-series climate surfaces to drive topographically distributed energy- and water-balance models. Hydrological Processes 13 (May 1998), 2003–2021.
Voogt, J., Oke, T., 2003. Thermal remote sensing of urban climates. Remote Sensing of Environment 86 (3), 370–384.
Wan, Z., 2008. New refinements and validation of the MODIS Land-Surface Temperature / Emissivity products. Remote sensing of Environment 112 (1), 59–74.
Wan, Z., Wang, P., Li, X., jan 2004. Using MODIS Land Surface Temperature and Normalized Difference Vegetation Index products for monitoring drought in the southern Great Plains, USA. International Journal of Remote Sensing 25 (1), 61–72.
Widlowski, J.-L., Robustelli, M., Disney, M., Gastellu-Etchegorry, J.-P., Lavergne, T., Lewis, P., North, P., Pinty, B., Thompson, R., Verstraete, M., mar 2008. The RAMI On-line Model Checker (ROMC): A web-based benchmarking facility for canopy reflectance models. Remote Sensing of Environment 112 (3), 1144–1150.
Widlowski, J. L., Taberner, M., Pinty, B., Bruniquel-Pinel, V., Disney, M., Fernandes, R., Gastellu-Etchegorry, J. P., Gobron, N., Kuusk, A., Lavergne, T., Leblanc, S., Lewis, P. E., Martin, E., Mottus, M., North, P. R. J., Qin, W., Robustelli, M., Rochdi, N., Ruiloba, R., Soler, C., Thompson, R., Verhoef, W., Verstraete, M. M., Xie, D., 2007. Third Radiation Transfer Model Intercomparison (RAMI) exercise: Documenting progress in canopy reflectance models. Journal of Geophysical Research Atmospheres 112 (9), 1–28.
Wu, P., Shen, H., Zhang, L., Göttsche, F.-M., 2015. Integrated fusion of multi-scale polar-orbiting and geostationary satellite observations for the mapping of high spatial and temporal resolution land surface temperature. Remote Sensing of Environment 156, 169–181.
Yang, K., Koike, T., Ishikawa, H., Kim, J., Li, X., Liu, H., Liu, S., Ma, Y., Wang, J., jan 2008. Turbulent Flux Transfer over Bare-Soil Surfaces: Characteristics and Parameterization. Journal of Applied Meteorology and Climatology 47 (1), 276–290.
Zhang, R., Tian, J., Su, H., Sun, X., Chen, S., Xia, J., oct 2008. Two Improvements of an Operational Two-Layer Model for Terrestrial Surface

Heat Flux Retrieval. Sensors 8 (10), 6165–6187.
Zhang, W., Gao, Y., 2011. Topographic correction algorithm for remotely sensed data accounting for indirect irradiance. International Journal of Remote Sensing 32 (7), 1807–1824.

List of Figures

Appendix

Dry bare soil EB equation:

In eq. 6, the dry soil ($_{s,dry}$) net radiation is

Generally, net radiation is expressed as:

$$Rn = K\downarrow - K\uparrow + L\downarrow - L\uparrow \tag{A.1}$$

where $K\downarrow$ being the surface downward shortwave radiative flux, $K\uparrow$ the surface upward shortwave flux, $L\downarrow$ the downward longwave flux and $L\uparrow$ the upward longwave flux. $K\uparrow$ is defined as the fraction of $K\downarrow$ at the surface that is reflected (albedo: α). $L\downarrow$ is results from whole atmosphere and clouds irradiance absorbed by the surface (εR_a). $L\uparrow$ is defined by the surface temperature from Stephan-Boltzmann law ($\varepsilon\sigma T^4$). Generally, Rn is calculated as:

$$Rn = (1-\alpha)Rg + \varepsilon R_a - \varepsilon\sigma T^4 \tag{A.2}$$

with α (-, dimensionless) being the albedo, ε (-) the emissivity, R_a (W.m^{-2}) the downward atmospheric radiation, and σ (W.m^{-2} K^{-4}) the Stefan-Boltzmann constant.

Then, $Rn_{s,dry}$ can be expressed as:

$$Rn_{s,dry} = (1-\alpha_s)Rg + \varepsilon_s R_a - \varepsilon_s\sigma T_{s,dry}^4 \tag{A.3}$$

with α_s (-, dimensionless) being the soil albedo and ε_s (-) the soil emissivity. The ground heat is commonly set to a fraction of soil net radiation:

$$Gd = C_G \times Rn_{s,dry} \tag{A.4}$$

with C_G (-) being set to 0.32 (Kustas and Daughtry, 1990). The dry soil sensible heat in eq. 6 is expressed as:

$$H_{s,dry} = \rho Cp\frac{T_{s,dry} - Ta}{rah_{s,dry}} \tag{A.5}$$

with ρ (Kg m^{-3}) being the air density, Cp (J Kg^{-1} K^{-1}) the air specific heat, Ta the air temperature (eq. 10) and $rah_{s,dry}$(s.m^{-1}) the aerodynamic resistance over dry bare soil.

Wet bare soil EB equation:

In eq. 7, the wet soil ($_{s,wet}$) net radiation is

$$Rn_{s,wet} = (1-\alpha_s)Rg + \varepsilon_s R_a - \varepsilon_s\sigma T_{s,wet}^4 \tag{A.6}$$

with the ground heat expressed as:

$$Gw = C_G \times Rn_{s,wet} \tag{A.7}$$

The wet soil sensible heat in eq. 7 is expressed as:

$$H_{s,wet} = \rho Cp\frac{T_{s,wet} - Ta}{rah_{s,wet}} \tag{A.8}$$

with $rah_{s,wet}$ (s.m^{-1}) being the aerodynamic resistance over wet bare soil. In eq. 7,$LE_{s,wet}$ (W.m^{-2}) the wet soil latent heat is expressed as:

$$LE_{s,wet} = \frac{\rho Cp}{\gamma}\frac{e_{sat}(T_{s,wet}) - (e_{sat}(Ta)\times\frac{Ha}{100})}{rah_{s,wet} + r_{v,min}} \tag{A.9}$$

with γ the psychrometric constant (Pa.K^{-1}) that relates the partial pressure of water in air to the air temperature, $e_{sat}(Ta)$ (Pa) the saturated vapor pressure at air temperature, $e_{sat}(Ts, wet)$ (Pa) the saturated vapor pressure at wet soil temperature, Ha (%) the air relative humidity (set to 25 s.m^{-1} (Moran et al., 1994)).

Stressed vegetation EB equation:

In eq. 8, the stressed vegetation ($_{v,dry}$) net radiation is:

$$Rn_{v,dry} = (1 - \alpha_v)Rg + \varepsilon_v R_a - \varepsilon_v \sigma T_{v,dry}^4 \tag{A.10}$$

with α_v (-) being the vegetation albedo, and ε_v (-) the vegetation emissivity. The vegetation sensible heat in eq. 8 is expressed as:

$$H_{v,dry} = \rho C p \frac{T_{v,dry} - Ta}{rah_{v,dry}} \tag{A.11}$$

with $H_{v,dry}$ (s.m^{-1}) the aerodynamic resistance over full-cover vegetation.

Well-watered vegetation EB equation:

In eq. 9, the well-watered vegetation ($_{v,wet}$) net radiation is:

$$Rn_{v,wet} = (1 - \alpha_v)Rg + \varepsilon_v R_a - \varepsilon_v \sigma T_{v,wet}^4 \tag{A.12}$$

The vegetation sensible heat in eq. 9 is expressed as:

$$H_{v,wet} = \rho C p \frac{T_{v,wet} - Ta}{rah_{v,wet}} \tag{A.13}$$

with $rah_{v,wet}$ (s.m^{-1}) the aerodynamic resistance over full-cover vegetation. In eq. 9, $LE_{v,wet}$ (W.m^{-2}) the vegetation latent heat is expressed as:

$$LE_{v,wet} = \frac{\rho C p}{\gamma} \frac{e_{sat}(T_{v,wet}) - (e_{sat}(Ta) \times \frac{Ha}{100})}{rah_{v,wet} + r_{v,min}} \tag{A.14}$$

with $e_{sat}(Tv, wet)$(Pa) the saturated vapor pressure at vegetation temperature. and rv,min the minimum stomatal resistance (set to 25 s.m^{-1} (Moran et al., 1994)).

The expressions of R_a, rah_s, rah_v, $e_{sat}(Ta)$, $e_{sat}(Ts)$ and $e_{sat}(Tv)$ are expressed as following:

In eq. A.3, A.6, A.10 and A.12 the downward atmospheric radiation is expressed as:

$$R_a = \varepsilon_a \sigma T a^4 \tag{A.15}$$

with ε_a (-) being the effective atmospheric emissivity. The emissivity of clear skies is estimated as in Brutsaert (1975) based on Kustas et al. (1994); Iziomon et al. (2003); Herrero and Polo (2012):

$$\varepsilon_a = 0.553(e_a/100)^{1/7} \tag{A.16}$$

with e_a the air vapor pressure computed as:

$$e_a = e_{sat}(Ta)(h_a/100) \tag{A.17}$$

In eq. A.9 and A.14 the saturated vapor pressure at temperature T is expressed as:

$$e_{sat}(T) = 611 \exp[17.27(T - 273.15)/(T - 35.9)] \tag{A.18}$$

In eq. A.5, A.8, A.9, A.11, A.13 and A.14 the component aerodynamic resistance rah for the soil or vegetation is estimated as in Choudhury et al. (1986):

$$rah = \frac{rah_0}{(1 + Ri)^\eta} \tag{A.19}$$

with rah_0(s.m^{-1}) being the neutral aerodynamic resistance, Ri (-) the Richardson number which represents the importance of free versus forced convection, and η (-) a coefficient set to 0.75 in unstable conditions (component temperature

larger than Ta) and 2 in stable conditions (component temperature lower than Ta). The Richardson number is computed as:

$$Ri = \frac{5gZ(T - Ta)}{TaU_a^2} \tag{A.20}$$

with T being the component temperature (Ts for rah_s and Tv for rah_v). The neutral rah_0 is computed as:

$$rah_0 = \frac{1}{k^2 U_a}\left[ln\left(\frac{Z-d}{Z0h}\right)\right]\left[ln\left(\frac{Z-d}{Z0m}\right)\right] \tag{A.21}$$

with k (-) being the von karman constant, U_a (m.s^{-1}) the wind speed measured at the height Z (m) and $Z0m$ (m) the momentum roughness. $Z0m$ is set to 0.003 m for rah_s (Yang et al., 2008; Stefan et al., 2015) and 0.1 m for rah_v (Allen et al., 1998). $Z0h$ is expressed as $Z0m$ divided by 10 (Allen et al., 1998).